Visualizing vibrationally resolved attosecond time delay in resonance-enhanced multiphoton ionization of NO molecules

Xing Li [1,*] Yong Liu [2,*] Dongdong Zhang,[1] Lanhai He [1] Sizuo Luo [1,†]
Chuan-Cun Shu [3,‡] and Dajun Ding[1,§]

[1]*Institute of Atomic and Molecular Physics, Jilin Provincial Key Laboratory of Applied Atomic
and Molecular Spectroscopy, Jilin University, Changchun 130012, China*
[2]*Department of Physics, Dalian University of Technology, Dalian 116024, China*
[3]*Hunan Key Laboratory of Nanophotonics and Devices, Hunan Key Laboratory of Super-Microstructure
and Ultrafast Process, School of Physics, Central South University, Changsha 410083, China*

We demonstrate a combined experimental and theoretical study to measure attosecond-resolved resonance-enhanced multiphoton ionization (REMPI) of NO molecules using the phase-locked strong 400-nm and weak 800-nm laser pulses. By performing the time-dependent wave-packet simulation, our results show that a vibrational-dependent REMPI occurs through two intermediate electronic states $A\,^2\Sigma^+$ and $B\,^2\Pi$, from which a molecular wave packet at different internuclear distances results in an ionization time delay up to 630 as. We find that the nonadiabatic coupling between electronic states $A\,^2\Sigma^+(\nu=2)$ and $B\,^2\Pi(\nu'=4)$ plays a crucial role in the angular-dependent phase variations of emitted electrons. This work extends the application of the REMPI technique to visualize the effect of vibrational motions of intermediate resonance states on the strong-field-induced ionization in attosecond timescales.

I. INTRODUCTION

Since Damon and Tomlinson's first observation in 1963 [1], the multiphoton ionization (MPI) of atoms and molecules by intense laser fields has attracted substantial attention in ultrafast strong-field physics [2,3]. It, in turn, results in a broad range of applications from laser-induced plasma generation [4,5], chemical diagnostics, and chiral recognition to laser filamentation [6,7], high-harmonic generation [8], and photoelectron spectroscopy [9]. The development of photoelectron spectroscopy has made it possible to observe the MPI phenomenon [10], for which the measured energy spectrum of photoelectrons consists of multiple peaks separated by the photon energies. Typically, there are two types of MPI: resonance-enhanced multiphoton ionization (REMPI) [11] and nonresonant multiphoton ionization (NRMPI) [12]. Due to the inclusion of the intermediate states, REMPI provides a selective and convenient means of detecting gas-phase species with small localized concentrations and is usually used to probe high-lying electronic states. While REMPI has been thoroughly studied [13,14], it still needs to be explored to gain insights into the REMPI of molecules due to the complexity arising from the nuclear motions. By separately measuring the energy or momentum spectra of the photoelectrons and the nuclei, it has been possible to observe vibrational-resolved

strong-field-induced phenomena, including bond softening [15], bond hardening [16], above-threshold dissociation [17], and Coulomb explosion imaging [18–20].

The reconstruction of attosecond beating by interference of two-photon transitions (RABBITT) [21–24] is a popular pump-probe technique widely used to determine photoionization delays with attosecond resolution. However, the nuclear motions in molecules can alter the potential barrier and influence the ionization process. Recent RABBITT experiments combined with theoretical calculations on N_2 molecules have confirmed that even small changes in molecular bond length can cause significant variations in the photoionization delay [25,26]. The nuclear-electronic coupling [27,28] is also crucial in determining the ionization delay of H_2 molecules [29,30]. Coincidence measurements of ionized electrons and corresponding fragments after dissociation have enabled the orientation-dependent ionization delay of polar molecules such as CO and NO [31,32]. The relative Wigner delay between two ionization sites can be tracked down to tens of attoseconds. The influence of resonance, particularly shape resonance [33], in single-photon ionization has also attracted extensive attention. Both experimental and theoretical results have shown that resonance can enhance ionization delays between different vibrational states and further influence the ionization delay at different emission angles [25,26,32,34,35]. In the case of multiphoton ionization of molecules, tracing the ionization dynamics from MPI is a great challenge for both experiments and theory because of the increasing complexity of ionization channels and the strong-field effect beyond the perturbation regime. Attosecond delay measurements have been made between forward and backward electrons emitted

*These authors contributed equally to this work.
†luosz@jlu.edu.cn
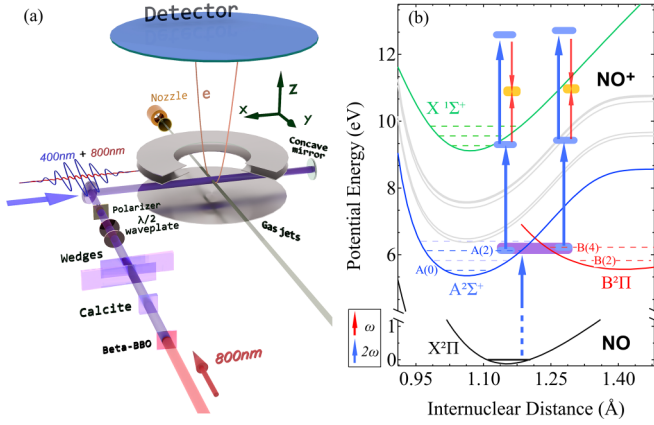‡cc.shu@csu.edu.cn
§dajund@jlu.edu.cn

FIG. 1. (a) Schematic diagram of the experimental setup. After the interaction of the laser field with NO molecules, the photoelectrons exit along the polarization axis y of the laser field, then are focused and imaged to the electron detector. (b) Potential curves of NO molecule: the colored blocks denote different stages in the two-color field photoionization process: two 400-nm photon resonant states (violet), stages of 400-nm ionization states (blue), and the interference for the sideband generation (orange).

from enantiomeric chiral molecules, and resonant states have been found to induce considerable time delays in experiments [36]. Additionally, the Wigner time delay has been observed upon ionizing H_2, CO in the molecular frame, and the spatial shifts of the electrons' birth positions after tunneling have been resolved [37,38]. In the below-threshold resonance ionization of NO molecules, the coupling between $A^2\Sigma^+$ and $B^2\Pi$ has been proven essential in two subcycle ionization dynamics under two-color (TC) laser fields [39–41].

This work explores the REMPI of NO molecules induced by strong ultrafast pulses to visualize the dependence of ionization time delay on vibrational motions of intermediate electronic states using a phase-locked strong 50 fs pulse centered at wavelength 400 nm and a weak 50 fs pulse centered at 800 nm. We measure the electron momenta and capture the phase variations of two ionization paths from different intermediate states. We perform time-dependent wave-packet simulations to gain insight into the underlying physics by considering both the vibrational and rotational degrees of freedom. Our measurements and theoretical analysis demonstrate that the nonadiabatic coupling between intermediate electronic states $A^2\Sigma^+$ and $B^2\Pi$ and their vibrational motions plays a role in the photoelectron spectra of REMPI, leading to a clear ionization time delay of several hundred attoseconds.

II. EXPERIMENTAL AND THEORETICAL METHODS

A. Experimental methods

Figure 1(a) illustrates our experiment scheme. We use two linearly polarized and phase-locked 50-fs laser pulses composed of the fundamental frequency of 800 nm and the second-harmonic frequency of 400 nm. The collinear configuration is used to maintain the stability of the relative phase $\Delta\phi$ between the two pulses [40–42]. We use a wire grid polarizer to make the polarization directions of the laser pulses parallel to the detector and adjust the intensity of the two laser pulses

by combining the half-wave plate. To ensure the validity of the attosecond delay measurement protocol in the multiphoton regime [42–44], we set the intensity of the fundamental pulse around 10^{11} W/cm^2, much weaker than its second harmonic around $(6–9) \times 10^{13}$ W/cm^2. To perform our experiments, we apply the two phase-controlled pulses to a gas jet of NO molecules and measure the ionized electrons by using a velocity map imaging spectrometer (VMIS) [45], as shown in Fig. 1(a). We take electron images between the 800- and 400-nm laser pulses at different relative phases. To avoid smearing out the asymmetry properties, we use the iterative Abel inversion method [46] to reconstruct the two-dimensional slice of the three-dimensional momentum distribution and extract the photoelectron spectra and angular distributions. The dependence of measured signals on the relative phase is obtained by precisely moving the fused silica wedges in our experiments with a step size of 0.04π (53.4 as) for the 800-nm laser field, corresponding to the scan length of around 4.2 fs in the electron momentum measurement.

B. Theoretical methods

The numerical simulations used to explain our experimental measurements are performed using a two-dimensional time-dependent quantum wave-packet method, which solves the time-dependent Schrödinger equation on a two-dimensional grid by considering both vibrational and rotational degrees of freedom. The model considers the REMPI from the ground electronic state $X^2\Pi$ of NO to the ionic ground state $X^1\Sigma^+$ of NO$^+$ through the intermediate excited electronic states $A^2\Sigma^+, B^2\Pi, C^2\Pi, D^2\Sigma, E^2\Sigma, F^2\Pi, G^2\Pi$, and $H^2\Sigma$ of NO [47], as shown in Fig. 1(b). The electronic continuum due to the ejection of the electron with the kinetic energy E_k is represented by a quasicontinuum, i.e., by a sufficiently large number N of discrete electronic states [48]. For convenience, we use $|X\rangle, |A\rangle, \ldots, |H\rangle$ to denote nine electronic states of NO and $|E_k\rangle$ to describe the ejection of the electron from the ionic continuum with the kinetic energy E_k, respectively. The time-dependent wave function of the system in the Born-Oppenheimer (BO) approximation can be written as

$$|\Psi(\mathbf{R}, t)\rangle = \sum_{i=X,A,\ldots,H} |\chi_i(\mathbf{R}, t)\rangle + \sum_{k=0}^{N} |\chi_{E_k}(\mathbf{R}; E_k, t)\rangle, \quad (1)$$

where $E_k = kE_N/N$ with the largest energy E_N, and $|\chi_i(\mathbf{R}, t)\rangle$ and $|\chi_{E_k}(\mathbf{R}; E_k, t)\rangle$ are the nuclear wave functions of the ith electronic state of the molecule NO and the nuclear wave function of the ground state of ionic NO$^+$ with kinetic energy E_k, respectively. $\mathbf{R} = \mathbf{R}(R, \theta)$ describes the nuclear coordinates with the nuclear distance R and angle θ between the molecular axis and the direction of the laser pulses.

By ignoring the nuclear-spin effect and considering the molecules initially in the ground rotational and vibrational state of the ground electronic state, the wave function $|\Psi(\mathbf{R}, t)\rangle \equiv |\Psi(R, \theta, t)\rangle$ can be obtained by solving the time-dependent Schrödinger equation (TDSE) with the Hamiltonian

$$\hat{\mathbf{H}} = -\frac{\hbar^2}{2m} \frac{\partial^2}{\partial R^2} \hat{\mathbf{I}} + \frac{\hat{\mathbf{J}}^2}{2mR^2} + \hat{\mathbf{V}}(R) + \hat{\mathbf{W}}(R, \theta, t), \quad (2)$$

where m denotes the reduced mass of the NO molecule, R the internuclear distance, and $\hat{\mathbf{J}}$ the angular momentum operator. $\hat{\mathbf{V}}(R)$ represents the potential energy operator that is a diagonal matrix composed of the elements $V_i(R)$ ($i = X, A, \ldots, H$) for nine bound electronic states and $V_{E_k}(R) = V_{E_0}(R) + E_k$ ($k = 1, \ldots, N$) for $N + 1$ ionized continuum states, where $V_{E_0}(R)$ corresponds to the potential energy surface of the ionic ground state of NO^+. $\hat{\mathbf{W}}(R, \theta, t)$ is the interaction potential, which describes the transitions between bound electronic states $|i\rangle$ and $|j\rangle$ through its off-diagonal elements $W_{ij}(R, t) = -\mu_{ij}(R) \cos\theta\mathcal{E}(t)$ for parallel transitions and $W_{ij}(R, t) = -\mu_{ij}(R) \sin\theta\mathcal{E}(t)$ for vertical transitions with the corresponding transition dipole moment μ_{ij} [40,49]. The transitions from the bound states $|i\rangle$ to the ionized continuum state $|E_k\rangle$ are assumed with a constant transition dipole moment μ_{iE_k} [40,49]. We also include the dynamic Stark shift of the bound electronic state $|i\rangle$ through the diagonal element of the interaction potential $W_{ii}(R, t) = -\frac{1}{2}[(\alpha_i^\perp(R) - \alpha_i^\parallel(R)) \cos^2\theta + \alpha_i^\perp(R)]\mathcal{E}^2(t)$, where $\alpha_i^\parallel(R)$ and $\alpha_i^\perp(R)$ refer to the corresponding parallel and perpendicular components of the polarizability tensor, respectively [50]. The technical details concerning solving the TDSE to obtain the bound-continuum wave function $|\Psi(R, \theta, t)\rangle$ can be found in previous works [40,49,51,52].

The photoelectron spectrum (PES) of observing the ejected electron with the kinetic energy E_k can be calculated by

$$\mathcal{P}(E_k) = \lim_{t \to \infty} \left| \int \sin\theta d\theta \int dR |\chi_{E_k}(R, \theta; E_k, t)\rangle \right|^2. \quad (3)$$

III. RESULTS AND DISCUSSIONS

We start our experiments by considering REMPI of NO molecules from the ground electronic state $X\,^2\Pi$ through a mixture of intermediate resonant states $A\,^2\Sigma^+$ and $B\,^2\Pi$, which interact with each other nonadiabatically due to Rydberg-valence coupling [39,40]. Figures 2(a) and 2(b) plot the variations of the experimentally measured and theoretically calculated PES to the time delay between pump and probe pulses. As shown in Fig. 1(b), the REMPI can occur in two different channels, which are excited from the ground electronic state to intermediate electronic states $A\,^2\Sigma^+(\nu = 2)$ and $B\,^2\Pi(\nu' = 4)$ by absorbing two 400-nm photons, corresponding to the violet blocks near 6.2 eV. After that, a weak 800-nm laser is introduced, and both sets of REMPI channels produce the sidebands in the same two routes: the first one to the ionic state by absorbing one 400-nm and one 800-nm photon, and the second one by absorbing two 400-nm photons while emitting one 800-nm photon through the continuum-continuum (CC) transition [53]. In the end, these two routes interfere and result in a sideband signal with an oscillation period of 1.33 fs [42–44]. The sideband signals associated with the two REMPI channels are denoted by the orange blocks in Fig. 1(b). We fit each sideband S_{SB}^n to extract the phase using the formula [21,54]

$$S_{SB}^n = A_n + B_n \cos[2\omega t + \varphi], \quad (4)$$

with $\varphi = \varphi_{laser} + \varphi_{cc} + \varphi_{mol}$, where φ_{laser} denotes the group delay of the pump laser pulses, φ_{cc} the phase delay during the CC transition, and φ_{mol} the phase delay accumulated
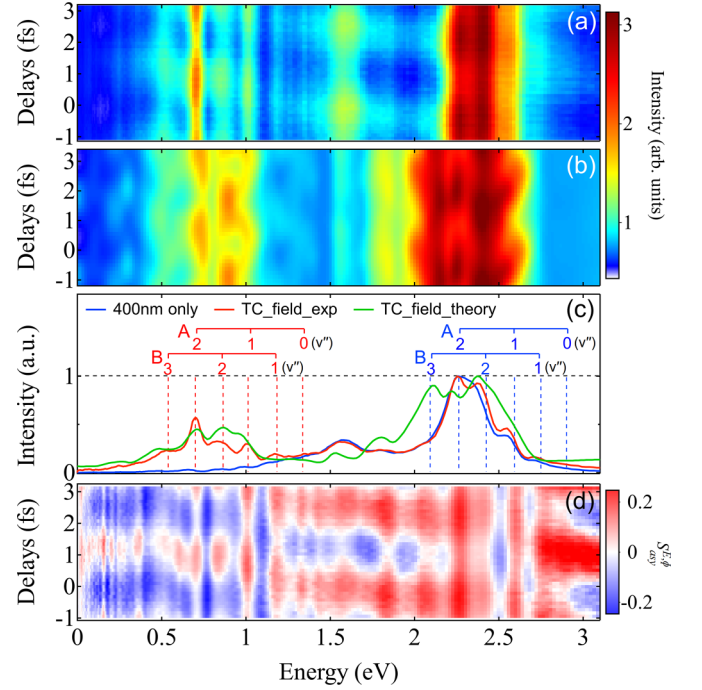

FIG. 2. (a) Measured and (b) simulated photoelectron spectra (logarithmic scale) integrated over the $+y$ axis as a function of the time delay between the 400- and 800-nm laser field. The color scales are normalized for comparison. (c) PES for 400 nm only (blue) and 400 nm + 800 nm (red), integrated by the phase period of the two-color laser fields. The letters A and B represent the resonance intermediate states of $A\,^2\Sigma^+(\nu = 2)$ and $B\,^2\Pi(\nu' = 4)$, respectively. ν'' label the vibrational quantum numbers corresponding to the different ionic vibrational states formed after the ionization; those two paths are assigned by horizontal short lines in blue (main peaks) and red (sidebands) color. (d) Asymmetry $S_{asy}^{E,\phi}$ calculated from experimental data corresponding to the photoelectron emitted at the $+y$ and $-y$ axis along the laser polarization.

from REMPI of molecules. In this case, it can further be divided into two terms with the phase $\varphi_{res} = \arg(M_{res})$ from resonance ionization and the phase φ_{Wigner} accumulated from the electron leaving the molecular potential. Our theoretical simulations in Fig. 2(b) exhibit the same period of oscillations as observed in the measured PES in phase-dependent traces. Figure 2(c) compares the experimentally measured and theoretically calculated PES induced by two pulses with the experimentally measured PES induced by a single pulse without using the weak 800-nm pulse. The PES is obtained by integration over the oscillation period. After ionization by a single 400-nm laser field, the PES has two distinct hump structures. In general, the observed kinetic energy of the photoelectron from REMPI is represented as

$$\epsilon = q\hbar\omega - (I_p - E_{A/B}) - (1 - \gamma)U_p, \quad (5)$$

where I_p is the ionization potential, $E_{A/B}$ the excitation energies of $A\,^2\Sigma^+$ and $B\,^2\Pi$ states, U_p the ponderomotive energy corresponding to the maximal Stark shift of a free electron in an oscillating electric field, γ the ratio of the ac Stark shift of the Rydberg resonant states to the ponderomotive energy, and γ equals 0.85 [40]. The high one around 2–3 eV comes from

the resonance pathway of the $2 + 2$ photon ionization from the vibrational state of $A\,^2\Sigma^+(\nu = 2)$ and the vibrational state of $B\,^2\Pi(\nu' = 4)$, and the lower one centered around 1.65 eV corresponds to the $2 + 2$ photon ionization through high-laying Rydberg states [39,55]. When the phase-locked 800 nm is added, more peaks with kinetic energy below 1.5 eV are observed. These peaks are assigned as the sideband (SB) peaks from two REMPI paths, absorbing three 400-nm photons and one 800-nm photon in one path and the other path absorbing four 400-nm photons and emitting one 800-nm photon, for which the resonance states are populated by absorbing two 400-nm photons, as illustrated in Fig. 1(b). The electron from the ionization of molecules exhibits a broad energy distribution that comes from different vibrational contributions, which can be seen in the experimentally measured PES. However, some overlapping exists between different channels when the 800-nm laser pulse is used. The main observed features can be reproduced well by the theoretical calculation with ac Stark shift of resonance states and free electrons in the laser field. In our simulations, we obtain the ponderomotive energy around 1 eV for the strong 400-nm pulse and the shifting of electron energy from REMPI around 0.15 eV compared to the field free electron. We plot the asymmetry ($S_{\mathrm{asy}}^{E,\phi}$) of the measured PES versus the time delay between the two pulses to assign the contribution states and to extract the ionization time delay [43], which is given by

$$S_{\mathrm{asy}}^{E,\phi} = (S_+^{E,\phi} - S_-^{E,\phi})/(S_+^{E,\phi} + S_-^{E,\phi}), \qquad (6)$$

where $S_+^{E,\phi}$ and $S_-^{E,\phi}$ are the measured photoelectrons emitted from the $+y$ and $-y$ axis of the laser polarization, respectively. The phase-dependent asymmetry of the photoelectron comes from the amplitude difference between two interfering ionization paths absorbing different numbers of photons to the same photoelectron peaks, which has been used to capture the attosecond ionization delay of atoms in the multiphoton regime [43]. Figure 2(d) displays the calculated phase-dependent $S_{\mathrm{asy}}^{E,\phi}$, which generally enhances the resolution of the spectrum and aids in identifying the origin of photoelectron peaks. Applying a weak 800-nm probe laser after the 400-nm pulse to the NO molecule, Fig. 2(c) shows that six distinct SB peaks are observed between 0.5 and 1.4 eV with an energy interval of approximately 0.14 eV. These peaks correspond to the higher energy hump emission of one 800-nm photon to the SB peak. However, the vibrational energy spacing in the ion state $X\,^1\Sigma^+$ for the NO molecule is $\sim 0.29\,\mathrm{eV}$, which implies that the ionization from the resonant $A\,^2\Sigma^+(\nu = 2)$ state by absorption of two 400-nm photons cannot be solely responsible for the observed peaks, as it would leave the NO ion in different vibrational states. It was shown that two-photon transition can populate both $A\,^2\Sigma^+$ and $B\,^2\Pi$ states, and the coupling between these states plays a significant role in the REMPI of NO molecules induced by two pulses [40,49]. Our numerical simulations in Fig. 2(c) reproduce the PES consisting of multiple peaks, which can be identified from the corresponding vibrational states by analyzing the time-dependent populations of vibrational states. Since the energies of $A\,^2\Sigma^+(\nu = 2)$ and $B\,^2\Pi(\nu' = 4)$ are 6.12 and 6.24 eV, respectively, the ionization occurs from the two resonant states, resulting in two well-resolved peaks around 2–3 eV.
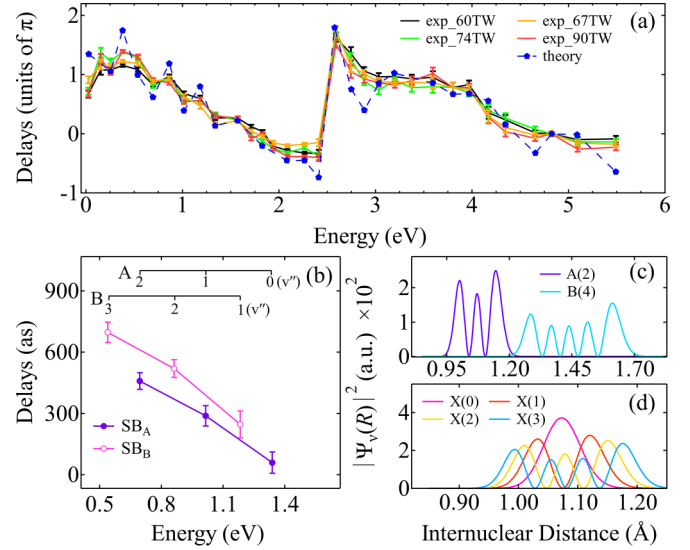

FIG. 3. Measured and simulated relative phase of the spectra of the NO molecule in the TC field. Correspondingly, (a) shows the retrieved relative phase resulting from fitting all the photoelectron peaks in the spectrum for experiment and simulation. (b) The phase of the six sidebands between 0.5 and 1.4 eV separated into two sets according the associated resonant states, $A\,^2\Sigma^+$ and $B\,^2\Pi$. (c) The absolute square of the different vibrational state wave functions of $A\,^2\Sigma^+(\nu = 2)$ and $B\,^2\Pi(\nu' = 4)$, and (d) for the ionic state $X\,^1\Sigma^+(\nu'' = 0, 1, 2, 3)$.

The sidebands between 0.5 and 1.4 eV, corresponding to the release to continuum via a CC transition at 800 nm, appear after the $2 + 2$ resonant ionization at 400 nm. We highlight these two different pathways by short horizontal lines in blue (main peaks) and red (sidebands) in Fig. 2(c). We can directly identify the underthreshold multiphoton resonant ionization dynamics at different electronic and vibrational states by analyzing the phase-delay difference between the two sidebands.

The time delay (τ) can be calculated using the formula $\tau = \varphi/(2\omega)$, which considers the phase shifts caused by measurement-induced contributions resulting from the coupling between the Coulomb field and the probing laser field [56], and the attosecond delay from the process of REMPI. Since φ_{laser} is the same for different vibrational states, and the difference in φ_{CC} is negligible, the phase variation can be monitored without any disturbances in a small energy range [22]. By conducting differential measurements of multiple vibrational channels, the measurement-induced delays (φ_{laser}, φ_{CC}) can be eliminated. It becomes possible to monitor the vibrational motions of the excited electronic states during excitation and ionization in attosecond timescales [25]. Figure 3(a) shows the remarkable agreement between the experimentally measured phase variation and the theoretically calculated one at different energies in the PES, showing the accuracy of the numerical simulation. Note that the phase variations in Fig. 3(a) are normalized to the nonresonance above threshold ionization (ATI) peak with the energy around 4.8 eV, where the phase is set at zero. We conduct four measurements with different pump laser intensities (6×10^{13}, 6.7×10^{13}, 7.4×10^{13}, and $9 \times 10^{13}\,\mathrm{W/cm^2}$) in our experiments. The results demonstrate that the phase variation remains

unaffected by varying the laser intensity, in agreement with our theoretical analysis, where the laser intensities were calibrated by measuring the electron energy shift resulting from the nonresonance ionization of Xe atoms [57].

To investigate the variation in ionization delay in the resonant channel, we narrowed our focus to the energy range 0.5–1.4 eV for the SB electron, as shown in Fig. 3(b). Two distinct sets of sidebands were identified, corresponding to transitions from $A^2\Sigma^+(\nu = 2)$ to $X^1\Sigma^+(\nu'' = 0, 1, 2)$ and $B^2\Pi(\nu' = 4)$ to $X^1\Sigma^+(\nu'' = 1, 2, 3)$. Each set consists of three peaks separated by an energy interval of approximately 0.3 eV, corresponding to different vibrational levels of the cation state $X^1\Sigma^+$. First, we examine the effect of the intermediate resonance states $A^2\Sigma^+$ and $B^2\Pi$ on the phase variations by measuring the ionization delay from the same vibrational levels ($\nu'' = 1, 2$), showing that the time delay between $A^2\Sigma^+$ and $B^2\Pi$ is around 50–60 as, respectively, which is within our measurement accuracy. Thus, the ionization delay influenced by the width of resonance states [58], where $\varphi_{\mathrm{Wigner}}$, φ_{CC} from two ionization paths of the same final vibrational state, is less than 60 as. Furthermore, we compare the attosecond ionization delay for the three vibrational levels from the same intermediate resonance state $A^2\Sigma^+$ or $B^2\Pi$. The measured results demonstrate that the ionization delay strongly depends on the vibrational states with a difference of around 420 as between vibrational states of $\delta\nu'' = 2$. The delay increases as the vibrational quantum number increases. We consider the electrons that were generated from the same intermediate resonance state. The difference was attributed to $\varphi_{\mathrm{Wigner}}$, which arises from the released electron wave packets scattering away from the molecular Coulomb potential. We can see that the time delay between vibrational states $\nu'' = 0$ and $\nu'' = 3$ reaches 630 as.

Due to the vibrational motions of the excited electronic states, the bond lengths of the molecules may change, resulting in an ionization delay on the order of hundreds of attoseconds between two vibration states, as observed in single-photon ionization of N_2 molecules [25]. Recent investigations have focused on the effect of ionization position by conducting orientation-dependent RABBITT measurements on CO molecules [59]. The measurements showed delays ranging from tens to around 160 as between the two ionization sites, highlighting the importance of ionization position on electron dynamics. The ionization delay observed in REMPI of NO molecules following two 400-nm photon resonances between the ground and exited states is caused by further ionization occurring at different internuclear distances. Figure 3(c) displays the absolute square of the wave function for the vibrational states $A^2\Sigma^+(\nu = 2)$ and $B^2\Pi(\nu' = 4)$. Ionization from the two intermediate resonant states occurs at different distances, namely, 1.15 and 1.28 Å. As we previously concluded, the main contribution to ionization delay corresponds to the different scattering position of the outgoing electrons with the Coulomb potential, i.e., the different $\varphi_{\mathrm{Wigner}}$. Figure 3(d) displays the probability density as a function of internuclear distance for different vibrational states ($\nu'' = 0, 1, 2, 3$) of the ion state $X^1\Sigma^+$, clearly showing the changes of the internuclear distance while the outgoing electron is moving away from the Coulomb potential, i.e., the right-hand side of the potential energy surface, from 1.07 to
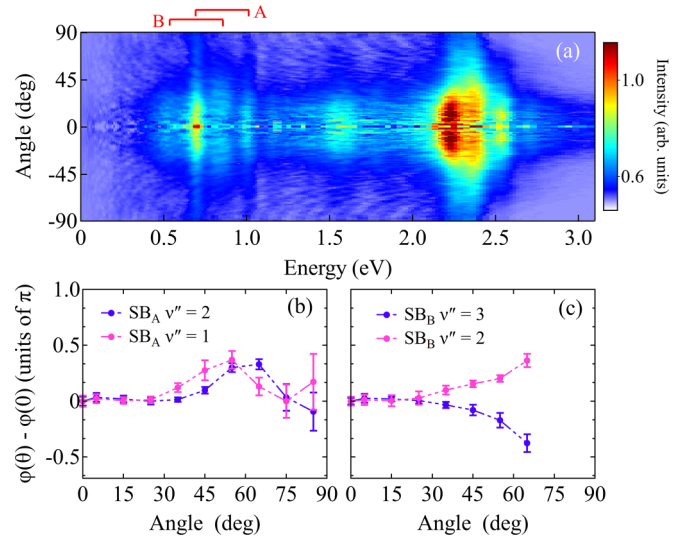

FIG. 4. (a) Measured phase integrated angular distribution of the photoelectron emitted from $+y$ axis. The $0°$ denotes the direction of laser polarization. (b) The comparison of the retrieved angle-dependent phases for the two sidebands of the $A^2\Sigma^+$ states. (c) Same as (b), but for the sidebands of the $B^2\Pi$ states. $\nu'' = 1, 2, 3$ indicates the different vibrational states of the NO^+ cation.

1.17 Å. Combining this observation with the phase variations in Fig. 3(b) implies that a new description is required to interpret the ionization phase in molecular REMPI by considering the coupling between nuclear and electronic motions, going beyond the description by using the Born-Oppenheimer approximation.

Different from our previous discussion regarding the phase difference between electrons from different vibrational levels, we now focus on the phase difference between emission angles. The angular distribution of electrons is plotted in Fig. 4(a), in which we only examine the angular distributions of sidebands, showing both the angular distributions for $A^2\Sigma^+$ to $X^1\Sigma^+$ at $\nu'' = 1, 2$ and $B^2\Pi$ to $X^1\Sigma^+$ at $\nu'' = 2, 3$. It should be noticed that the angular distributions from different vibrational states of the same intermediate electronic state exhibit similar distributions, indicating that the electronic transitions between states are dominant. The angular dependence of the phase $\varphi_{\mathrm{res}}(\theta) = \arg(M_{\mathrm{res}}(\theta))$ is sensitive to the anisotropic nature of the molecular Coulomb potential and the transition between resonance states to $X^1\Sigma^+$. Figures 4(b) and 4(c) show the measured angular-dependent ionization delay from $A^2\Sigma^+$ and $B^2\Pi$ states, where the delay is normalized to be zero at $0°$. We can see from Fig. 4(b) that the electrons from the two final vibrational levels exhibit a similar angular dependence, where the phase remains flat from $0°$ to around $30°$, followed by a slight increase to around $65°$ and then decreases to $90°$. It implies that the electronic transitions between states determine the final distributions.

This situation becomes even more complex when the electrons are emitted from the resonance state $B^2\Pi$. The angular-dependent phase variation for $\nu'' = 2$ shows similar distributions to those of $A^2\Sigma^+$, where the phase remains unchanged between $0°$ to around $30°$ and then increases until around $65°$. The angular-dependent phase variation for $\nu'' = 3$

exhibits an entirely different behavior, where the phase variation is flat until $30°$ and then decreases until around $65°$. These two peaks imply that there are almost no electron emissions for the angle larger than $65°$. As previously mentioned, the REMPI process of NO molecules is significantly influenced by the coupling between $A\,^2\Sigma^+$ and $B\,^2\Pi$ states. Hence, we infer that the angular dependence for $\nu'' = 2$, where the final energy falls between the electrons from $A\,^2\Sigma^+$ to $X\,^1\Sigma^+$ at $\nu'' = 1, 2$, is highly influenced by the transition from $A\,^2\Sigma^+$ to $X\,^1\Sigma^+$. On the other hand, the distinct distribution observed for $\nu'' = 3$ comes from the transition of $B\,^2\Pi$ to $X\,^1\Sigma^+$. This observation is consistent with the previous finding that ionization from different emission energy exhibits varying effects due to the coupling between $A\,^2\Sigma^+$ and $B\,^2\Pi$ states.

IV. CONCLUSION

We experimentally and theoretically demonstrated the REMPI of NO molecules with attosecond resolution to investigate the ionization time delay of vibrationally resolved PES. We found that ionization times differ for electrons emitted from different final vibrational states at different internuclear distances, with a time delay above 630 as. We performed time-dependent quantum wave-packet simulations by including all of the intermediate states to explain our experimental measurements, showing that even small changes in bond length due to vibrational motion could significantly affect the ionization delay. We concluded that the resonance states $A\,^2\Sigma^+(\nu = 2)$ and $B\,^2\Pi(\nu' = 4)$ may only weakly affect the angular integral delay. By analyzing the angular-dependent emission delay, we investigated the nonadiabatic coupling between the two electronic states and observed an energy-dependent influence for electrons with different final energies. This work provides a promising avenue for observing the nonadiabatic coupling and vibrational effects in the ionization time delay of molecules.

[1] E. K. Damon and R. G. Tomlinson, Observation of ionization of gases by a ruby laser, Appl. Opt. **2**, 546 (1963).

[2] S. W. Allendorf and A. Szöke, High-intensity multiphoton ionization of H_2, Phys. Rev. A **44**, 518 (1991).

[3] K. Harumiya, H. Kono, Y. Fujimura, I. Kawata, and A. D. Bandrauk, Intense laser-field ionization of H_2 enhanced by two-electron dynamics, Phys. Rev. A **66**, 043403 (2002).

[4] S. L. Chin, H. L. Xu, Q. Luo, F. Théberge, W. Liu, J. F. Daigle, Y. Kamali, P. T. Simard, J. Bernhardt, S. A. Hosseini, M. Sharifi, G. Méjean, A. Azarm, C. Marceau, O. Kosareva, V. P. Kandidov, N. Aközbek, A. Becker, G. Roy, P. Mathieu *et al.*, Filamentation "remote" sensing of chemical and biological agents/pollutants using only one femtosecond laser source, Appl. Phys. B **95**, 1 (2009).

[5] L. J. Radziemski, T. R. Loree, D. A. Cremers, and N. M. Hoffman, Time-resolved laser-induced breakdown spectrometry of aerosols, Anal. Chem. **55**, 1246 (1983).

[6] H. Li, W. Chu, H. Xu, Y. Cheng, S.-L. Chin, K. Yamanouchi, and H.-B. Sun, Simultaneous identification of multi-combustion-intermediates of alkanol-air flames by femtosecond filament excitation for combustion sensing, Sci. Rep. **6**, 27340 (2016).

[7] A. Braun, G. Korn, X. Liu, D. Du, J. Squier, and G. Mourou, Self-channeling of high-peak-power femtosecond laser pulses in air, Opt. Lett. **20**, 73 (1995).

[8] P. Maine, D. Strickland, P. Bado, M. Pessot, and G. Mourou, Generation of ultrahigh peak power pulses by chirped pulse amplification, IEEE J. Quantum Electron. **24**, 398 (1988).

[9] D. Villarejo, R. R. Herm, and M. G. Inghram, Measurement of threshold electrons in the photoionization of Ar, Kr, and Xe, J. Chem. Phys. **46**, 4995 (1967).

[10] G. S. Voronov and N. B. Delone, Ionization of the xenon atom by the electric field of ruby laser emission, Sov. Phys. JETP **1**, 66 (1965).

[11] R. R. Freeman, P. H. Bucksbaum, H. Milchberg, S. Darack, D. Schumacher, and M. E. Geusic, Above-Threshold Ionization with Subpicosecond Laser Pulses, Phys. Rev. Lett. **59**, 1092 (1987).

[12] G. Petite, F. Fabre, P. Agostini, M. Crance, and M. Aymar, Nonresonant multiphoton ionization of cesium in strong fields: Angular distributions and above-threshold ionization, Phys. Rev. A **29**, 2677 (1984).

[13] P. Ge, M. Han, M.-M. Liu, Q. Gong, and Y. Liu, Probing time delays and coherent imaging of multiphoton resonant ionization, Phys. Rev. A **98**, 013409 (2018).

[14] J. Yu, W. Hu, X. Li, P. Ma, L. He, F. Liu, C. Wang, S. Luo, and D. Ding, Contribution of resonance excitation on ionization of OCS molecules in strong laser fields, J. Phys. B: At. Mol. Opt. Phys. **50**, 235602 (2017).

[15] P. H. Bucksbaum, A. Zavriyev, H. G. Muller, and D. W. Schumacher, Softening of the H_2^+ Molecular Bond in Intense Laser Fields, Phys. Rev. Lett. **64**, 1883 (1990).

[16] G. Yao and S.-I. Chu, Molecular-bond hardening and dynamics of molecular stabilization and trapping in intense laser pulses, Phys. Rev. A **48**, 485 (1993).

[17] A. Giusti-Suzor, X. He, O. Atabek, and F. H. Mies, Above-Threshold Dissociation of H_2^+ in Intense Laser Fields, Phys. Rev. Lett. **64**, 515 (1990).

[18] B. D. Esry, A. M. Sayler, P. Q. Wang, K. D. Carnes, and I. Ben-Itzhak, Above Threshold Coulomb Explosion of Molecules in Intense Laser Pulses, Phys. Rev. Lett. **97**, 013003 (2006).

[19] X. Li, X. Yu, P. Ma, X. Zhao, C. Wang, S. Luo, and D. Ding, Ultrafast Coulomb explosion imaging of molecules and molecular clusters, Chin. Phys. B **31**, 103304 (2022).

[20] X. Zhao, T. Xu, X. Yu, D. Ren, X. Zhang, X. Li, P. Ma, C. Wang, D. Zhang, Q. Wang, X. Hu, S. Luo, Y. Wu, J. Wang, and D. Ding, Tracking the nuclear movement of the carbonyl sulfide cation after strong-field ionization by time-resolved Coulomb-explosion imaging, Phys. Rev. A **103**, 053103 (2021).

[21] K. Klünder, J. M. Dahlström, M. Gisselbrecht, T. Fordell, M. Swoboda, D. Guénot, P. Johnsson, J. Caillat, J. Mauritsson, A. Maquet, R. Taïeb, and A. L'Huillier, Probing Single-Photon Ionization on the Attosecond Time Scale, Phys. Rev. Lett. **106**, 143002 (2011).

[22] J. M. Dahlström, D. Guénot, K. Klünder, M. Gisselbrecht, J. Mauritsson, A. L'Huillier, A. Maquet, and R. Taïeb, Theory of attosecond delays in laser-assisted photoionization, Chem. Phys. **414**, 53 (2013).

[23] M. Bertolino and J. M. Dahlström, Multiphoton interaction phase shifts in attosecond science, Phys. Rev. Res. **3**, 013270 (2021).

[24] M. Li, H. Wang, X. Li, J. Wang, J. Zhang, X. San, P. Ma, Y. Lu, Z. Liu, C. Wang, Y. Yang, S. Luo, and D. Ding, Stable attosecond beamline equipped with high resolution electron and XUV spectrometer based on high-harmonics generation, J. Electron Spectrosc. Relat. Phenom. **263**, 147287 (2023).

[25] S. Nandi, E. Plésiat, S. Zhong, A. Palacios, D. Busto, M. Isinger, L. Neoričić, C. L. Arnold, R. J. Squibb, R. Feifel, P. Decleva, A. L'Huillier, F. Martín, and M. Gisselbrecht, Attosecond timing of electron emission from a molecular shape resonance, Sci. Adv. **6**, eaba7762 (2020).

[26] V. J. Borràs, J. González-Vázquez, L. Argenti, and F. Martín, Attosecond photoionization delays in the vicinity of molecular Feshbach resonances, Sci. Adv. **9**, eade3855 (2023).

[27] M. Kowalewski, K. Bennett, J. R. Rouxel, and S. Mukamel, Monitoring Nonadiabatic Electron-Nuclear Dynamics in Molecules by Attosecond Streaking of Photoelectrons, Phys. Rev. Lett. **117**, 043201 (2016).

[28] S. Patchkovskii, J. Benda, D. Ertel, and D. Busto, Theory of nuclear motion in RABBITT spectra, Phys. Rev. A **107**, 043105 (2023).

[29] L. Cattaneo, J. Vos, R. Y. Bello, A. Palacios, S. Heuser, L. Pedrelli, M. Lucchini, C. Cirelli, F. Martín, and U. Keller, Attosecond coupled electron and nuclear dynamics in dissociative ionization of H_2, Nat. Phys. **14**, 733 (2018).

[30] A. L. Wang, V. V. Serov, A. Kamalov, P. H. Bucksbaum, A. Kheifets, and J. P. Cryan, Role of nuclear-electronic coupling in attosecond photoionization of H_2, Phys. Rev. A **104**, 063119 (2021).

[31] J. Vos, L. Cattaneo, S. Patchkovskii, T. Zimmermann, C. Cirelli, M. Lucchini, A. Kheifets, A. S. Landsman, and U. Keller, Orientation-dependent stereo Wigner time delay and electron localization in a small molecule, Science **360**, 1326 (2018).

[32] F. Holzmeier, J. Joseph, J. C. Houver, M. Lebech, D. Dowek, and R. R. Lucchese, Influence of shape resonances on the angular dependence of molecular photoionization delays, Nat. Commun. **12**, 7343 (2021).

[33] M. N. Piancastelli, The neverending story of shape resonances, J. Electron Spectrosc. Relat. Phenom. **100**, 167 (1999).

[34] M. Huppert, I. Jordan, D. Baykusheva, A. von Conta, and H. J. Wörner, Attosecond Delays in Molecular Photoionization, Phys. Rev. Lett. **117**, 093001 (2016).

[35] A. Kamalov, A. L. Wang, P. H. Bucksbaum, D. J. Haxton, and J. P. Cryan, Electron correlation effects in attosecond photoionization of CO_2, Phys. Rev. A **102**, 023118 (2020).

[36] S. Beaulieu, A. Comby, A. Clergerie, J. Caillat, D. Descamps, N. Dudovich, B. Fabre, R. Géneaux, F. Légaré, S. Petit, B. Pons, G. Porat, T. Ruchon, R. Taïeb, V. Blanchet, and Y. Mairesse, Attosecond-resolved photoionization of chiral molecules, Science **358**, 1288 (2017).

[37] D. Trabert, S. Brennecke, K. Fehre, N. Anders, A. Geyer, S. Grundmann, M. S. Schöffler, L. P. H. Schmidt, T. Jahnke, R. Dörner, M. Kunitski, and S. Eckart, Angular dependence of the Wigner time delay upon tunnel ionization of H_2, Nat. Commun. **12**, 1697 (2021).

[38] Z. Guo, P. Ge, Y. Fang, Y. Dou, X. Yu, J. Wang, Q. Gong, and Y. Liu, Probing molecular frame wigner time delay and electron wavepacket phase structure of CO molecule, Ultrafast Sci. **2022**, 9802917 (2022).

[39] B. Wang, B. Liu, Y. Wang, and L. Wang, Field modulation of Rydberg-state populations of NO studied by femtosecond time-resolved photoelectron imaging, Phys. Rev. A **81**, 043421 (2010).

[40] W. Hu, Y. Liu, S. Luo, X. Li, J. Yu, X. Li, Z. Sun, K.-J. Yuan, A. D. Bandrauk, and D. Ding, Coherent interference of molecular electronic states in NO by two-color femtosecond laser pulses, Phys. Rev. A **99**, 011402(R) (2019).

[41] W. Hu, X. Li, H. Zhao, W. Li, Y. Lei, X. Kong, A. Liu, S. Luo, and D. Ding, Sub-optical-cycle electron dynamics of NO molecules: The effect of strong laser field and Coulomb field, J. Phys. B: At. Mol. Opt. Phys. **53**, 084002 (2020).

[42] L. J. Zipp, A. Natan, and P. H. Bucksbaum, Probing electron delays in above-threshold ionization, Optica **1**, 361 (2014).

[43] X. Gong, C. Lin, F. He, Q. Song, K. Lin, Q. Ji, W. Zhang, J. Ma, P. Lu, Y. Liu, H. Zeng, W. Yang, and J. Wu, Energy-Resolved Ultrashort Delays of Photoelectron Emission Clocked by Orthogonal Two-Color Laser Fields, Phys. Rev. Lett. **118**, 143203 (2017).

[44] X. Song, G. Shi, G. Zhang, J. Xu, C. Lin, J. Chen, and W. Yang, Attosecond Time Delay of Retrapped Resonant Ionization, Phys. Rev. Lett. **121**, 103201 (2018).

[45] A. T. J. B. Eppink and D. H. Parker, Velocity map imaging of ions and electrons using electrostatic lenses: Application in photoelectron and photofragment ion imaging of molecular oxygen, Rev. Sci. Instrum. **68**, 3477 (1997).

[46] M. J. J. Vrakking, An iterative procedure for the inversion of two-dimensional ion/photoelectron imaging experiments, Rev. Sci. Instrum. **72**, 4084 (2001).

[47] F. R. Gilmore, Potential energy curves for N_2, NO, O_2 and corresponding ions, J. Quant. Spectrosc. Radiat. Transfer **5**, 369 (1965).

[48] C. Meier and V. Engel, Interference Structure in the Photoelectron Spectra Obtained from Multiphoton Ionization of Na_2 with a Strong Femtosecond Laser Pulse, Phys. Rev. Lett. **73**, 3207 (1994).

[49] Y. Liu, W. H. Hu, S. Z. Luo, K. J. Yuan, Z. G. Sun, A. D. Bandrauk, and D. J. Ding, Vibrationally resolved above-threshold ionization in NO molecules by intense ultrafast

two-color laser pulses: An experimental and theoretical study, Phys. Rev. A **100**, 023404 (2019).

[50] J.-W. Hu and Y.-C. Han, Investigation of photoassociation with full-dimensional thermal-random-phase wavefunctions, J. Phys. B: At. Mol. Opt. Phys. **155**, 064108 (2021).

[51] C.-C. Shu, J. Yu, K.-J. Yuan, W.-H. Hu, J. Yang, and S.-L. Cong, Stimulated Raman adiabatic passage in molecular electronic states, Phys. Rev. A **79**, 023418 (2009).

[52] C.-C. Shu, K.-J. Yuan, W.-H. Hu, and S.-L. Cong, Resonance-enhanced above-threshold ionization of polar molecules induced by ultrashort laser pulses, J. Phys. B: At. Mol. Opt. Phys. **41**, 065602 (2008).

[53] A. S. Kheifets and A. W. Bray, RABBITT phase transition across the ionization threshold, Phys. Rev. A **103**, L011101 (2021).

[54] P. M. Paul, E. S. Toma, P. Breger, G. Mullot, F. Augé, P. Balcou, H. G. Muller, and P. Agostini, Observation of a train of attosecond pulses from high harmonic generation, Science **292**, 1689 (2001).

[55] W. Guo, Y. Wang, and Y. Li, Femtosecond photoelectron imaging of NO at 410 nm, Optik **161**, 151 (2018).

[56] C. Palatchi, J. M. Dahlström, A. S. Kheifets, I. A. Ivanov, D. M. Canaday, P. Agostini, and L. F. DiMauro, Atomic delay in helium, neon, argon and krypton, J. Phys. B: At. Mol. Opt. Phys. **47**, 245003 (2014).

[57] O. Hüter and F. Temps, Note: Energy calibration of a femtosecond photoelectron imaging detector with correction for the ponderomotive shift of atomic ionization energies, Rev. Sci. Instrum. **88**, 046101 (2017).

[58] L. Neoričić, D. Busto, H. Laurell, R. Weissenbilder, M. Ammitzböll, S. Luo, J. Peschel, H. Wikmark, J. Lahl, S. Maclot, R. J. Squibb, S. Zhong, P. Eng-Johnsson, C. L. Arnold, R. Feifel, M. Gisselbrecht, E. Lindroth, and A. L'Huillier, Resonant two-photon ionization of helium atoms studied by attosecond interferometry, Front. Phys. **10**, 964586 (2022).

[59] J. Rist, K. Klyssek, N. M. Novikovskiy, M. Kircher, I. Vela-Pérez, D. Trabert, S. Grundmann, D. Tsitsonis, J. Siebert, A. Geyer, N. Melzer, C. Schwarz, N. Anders, L. Kaiser, K. Fehre, A. Hartung, S. Eckart, L. P. H. Schmidt, M. S. Schöffler, V. T. Davis *et al.*, Measuring the photoelectron emission delay in the molecular frame, Nat. Commun. **12**, 6657 (2021).